A sub-kHz mechanical resonator passively cooled to 6 mK

Everdingen, L.R. van; Plugge, J.; Fuchs, T.; Stolpe, G. van de; Benali, D.; Jong, T. de; ... ; Oosterkamp, T.H.

A Sub-kHz Mechanical Resonator Passively Cooled to 6 mK

Loek van Everdingen,[1,*] Jaimy Plugge,[1,*] Tim M. Fuchs,[1,2] Guido L. van de Stolpe,[1,3]
Dalal Benali,[1] Thijmen de Jong,[1] Jasper Bijl,[1] Wim A. Bosch,[1] and Tjerk H. Oosterkamp[1,†]

[1]*Leiden Institute of Physics, Leiden University, P.O. Box 9504, 2300 RA Leiden, The Netherlands.*
[2]*School of Physics and Astronomy, University of Southampton, SO17 1BJ, Southampton, United Kingdom.*
[3]*E. L. Ginzton Laboratory, Stanford University, 348 Via Pueblo, Stanford, California, United States of America*

(Dated: October 29, 2025)

Fundamental tests of quantum mechanics, such as the generation of non-classical states and tests of wavefunction collapse models, are performed on increasingly larger size and mass scales. Highly coherent mechanical resonators, which also prove invaluable in ultrasensitive microscopy methods, are essential tools towards these efforts. Studying these resonators in a thermal equilibrium state at millikelvin temperatures provides a promising path to increase their coherence time. Here, we passively cool a 700 Hz massive (1.5 ng) mechanical cantilever down to $6.1(4)\mathrm{mK}$ by means of nuclear demagnetization, as confirmed by detecting its thermal motion via a lock-in based detection scheme. At the lowest temperatures the thermal motion of the resonator is still clearly distinguishable from the background noise. Our data analysis confirms that at these temperatures the motion is still thermally distributed. These results pave the way for passive cooling low-frequency resonators to the sub-milllikelvin regime, which would enable new tests of quantum mechanics and advances in ultrasensitive force detection.

The quantum-to-classical boundary addresses fundamental questions concerning wavefunction collapse [1, 2] and the interaction between quantum mechanics and gravity [3–5]. Despite of significant efforts, in terms of mass, there is currently still a large discrepancy between the largest object that was brought in a spatial superposition [6, 7] and the smallest objects that served as a source of gravity [8, 9]. Essential tools towards closing this quantum-to-classical gap are mechanical resonators with favorable properties, such as high Q-factors [10, 11], low force noise [12–14] and good displacement sensitivity [15, 16]. These properties tend to improve at lower resonator temperature and consequently experiments are generally carried out at cryogenic temperatures [17].

To reach such low temperatures, both active and passive forms of cooling are being explored. Active cooling requires continuous driving of a mode, such as feedback cooling [18] or sideband cooling [19], and has been employed to cool mechanical resonators in a wide range of frequencies into their ground state [11, 20–22]. However, active cooling does not improve the force noise of the ground state because it does not lower the temperature of the environment. Moreover, it is undesirable in experiments probing quantum systems, as it disturbs a system from mechanical equilibrium via the external drive. On the contrary, passive cooling leaves a mechanical system in thermal equilibrium, once cold. It was first used to cool GHz systems to their ground state at the operation temperature of a dilution refrigerator [23]. A widely-applied form of passive cooling is nuclear demagnetization, which has been used to cool microelectronics below 1 mK [24, 25], and was recently employed to cool a 15 MHz device into its motional ground state [26].

However, bringing sub-kHz mechanical probes to sub-mK temperatures while leaving them in thermal equilibrium remains a formidable challenge [27]. If achieved, it has the potential to improve the Q-factor of highly-coherent mechanical resonators by mitigating mechanical loss channels [28, 29]. Mechanical sensors with a high Q-factor and low-force noise find application in the aforementioned experiments on the quantum-to-classical boundary and in ultrasensitive detection, including extreme mass sensing [8, 9] and acceleration detection [30]. Additionally, they prove an essential tool to test models of wave function collapse, such as Diosí-Penrose models and Continuous Spontaneous Localization (CSL) [31–33].

In this work, we apply nuclear demagnetization to cool a $1.5\,\mathrm{ng}$ mechanical resonator to $6.1(4)\,\mathrm{mK}$. By introducing a lock-in detection scheme that tracks the resonator energy, we are able to verify the thermal equilibrium nature of its state through the direct observation of Boltzmann energy statistics. To our knowledge, this is the first observation of the equilibrium motion of a massive mechanical resonator in the Hz- to kHz-regime below the $20\,\mathrm{mK}$ base temperature of conventional dilution refrigerators.

A. Experimental setup

The experimental setup used in this work was originally designed for magnetic resonance force microscopy (MRFM) at low temperatures (see Fig. 1). A soft silicon cantilever [34] with a magnetic tip ($Nd_2Fe_{14}B$ sphere, 7.3 μm diameter) is suspended above a pickup loop in a pulse tube cryogen-free dilution refrigerator (Leiden Cryogenics CF-1200). To minimize mechanical vibrations, the experiment is mounted on a mass-spring suspension system hanging inside the dilution refrigerator. The cantilever exhibits a resonance frequency $\omega_0 \approx 2\pi \times 700\,\mathrm{Hz}$ and a spring constant of $26\,\mu\mathrm{Nm}^{-1}$. Magnetic flux induced in the pickup loop generates a current in a SQUID input coil of a two-stage readout SQUID (Magnicon NC-1 Integrated Two-Stage Current Sensor), and hence a voltage signal. Precise positioning of the cantilever

* These authors share first authorship and contributed equally.
† Contact author: oosterkamp@physics.leidenuniv.nl

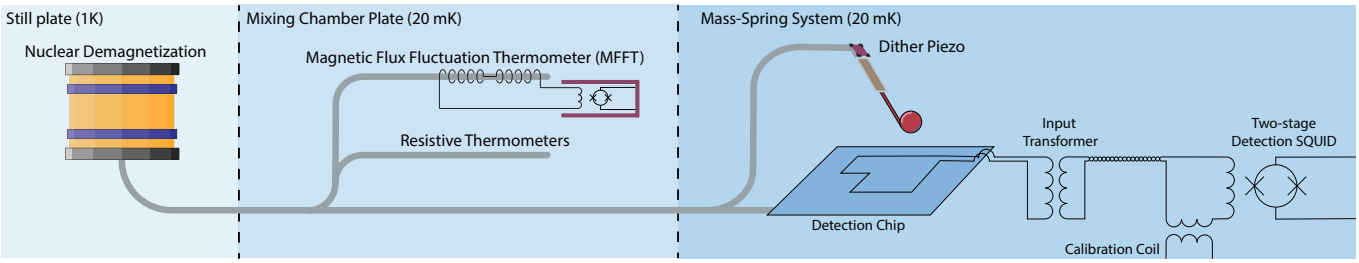

FIG. 1. Schematic illustration of the setup used for this work. A thermally isolated silver wire is linked to the nuclear demagnetization stage and connects different parts of the experiment, notably the cantilever, detection chip and input transformer to a temperature below the base temperature of the dilution refrigerator at 20mK. The lower right corner of the schematic shows the circuit that is used for the detection and calibration of the cantilever motion. The position inside the dilution refrigerator of different parts is indicated. In the center part the MFFT is illustrated inside its lead shielding (purple). The lower part shows the cantilever suspended above the detection circuit.

is achieved using a piezomotor system comprising three independently controllable spindles actuated by slip-stick piezomotors. Oscillations of the cantilever can be driven electrically through a dither piezo that excites the cantilever base. The amplitude of the cantilever oscillations can be calibrated through a calibration coil which excites the cantilever magnetically, and which is located between the pickup loop and the readout SQUID input coil. The cantilever frequency varies at different positions due to local forces acting on the cantilever. The local forces cause a change in the effective stiffness k_{eff}, which causes variations in the effective resonance frequency ω_{eff}.

To achieve cooling of the cantilever below the base temperature of the dilution refrigerator ($\sim$ 20 mK), we thermally anchor both the cantilever and the detection chip to a $PrNi_5$ nuclear demagnetization stage using a silver wire (contrary to previous work where only the cantilever was connected [29]). Crucially,the silver strip is routed along the mass-spring system using thermally isolating clamps, so that it is mechanically, but not thermally, connected to each mass. This allows the wire to reach sub-millikelvin temperatures (the mass-spring system is thermalized at $\sim$ 20 mK), while retaining optimal vibration isolation [29]. Thermal isolation between the detection chip and the sample holder is achieved by placing the detection chip on top of a machined Macor® plate.

In order to accurately determine the temperature of the environment, three thermometers are connected to the silver wire. We use two fast and accurate resistance thermometers for temperatures between 15 mK and 1 K, and a magnetic flux fluctuation thermometer (MFFT) for lower temperatures, which induces minimal heat dissipation [35]. The MFFT consists of a gradiometric coil wound around the silver wire that picks up magnetic fluctuations induced by Johnson-Nyquist noise, which is measured using a second Magnicon SQUID [29]. Details on the thermometer calibration procedure can be found in the supplementary material [36].

We directly infer the cantilever temperature by detecting its thermal motion through the AC magnetic flux signal induced in the SQUID pickup loop [37]. This measurement of the cantilever motion is minimally invasive, with added dissipation in principle only limited by the coupling between the cantilever and the detector. We measure the flux-to-voltage conversion parameter κ by driving the cantilever with an oscillating test flux generated by a calibration coil (see Fig. 1) and measuring the resulting flux through the pickup coil [29]. Note that here we only consider magnetic interactions, neglecting possible electrostatic contributions (e.g. due to residual charges on the cantilever tip). A detailed discussion on the calibration procedure can be found in the supplementary material [36].

This work presents experiments in two different cooldown cycles of the dilution refrigerator, for which the respective measurement parameters are presented in table I. In each cycle, we start by varying the coupling between the detection circuit and the cantilever before turning on the nuclear demagnetization. The resulting conversion parameters κ are given in appendix E. In both cooldown cycles, the cantilever is more than 10 μm away from the surface of the detection chip while measuring.

B. Determination of the Cantilever Temperature through its Thermal Motion

To extract the cantilever temperature, we introduce a lock-in-based detection scheme that enables real-time tracking of the cantilever energy (here executed in post-processing, see supplementary material [36] for details on the analysis). Such an energy time trace facilitates immediate insight into the resonator thermodynamics (see Fig. 2b) which we use here to verify the thermally limited nature of its motion (Fig. 2c). This method offers a clear and intuitive way to analyze the cantilever signal, and can be considered complementary to frequency domain methods [29].

The thermal motion of the cantilever is given by $\langle x\rangle^2 = \mathrm{k}_B T/k$, where $\langle x\rangle^2$ is the time-averaged amplitude of the cantilever displacement, and k is the cantilever stiffness (by invoking the equipartition theorem [38]). The

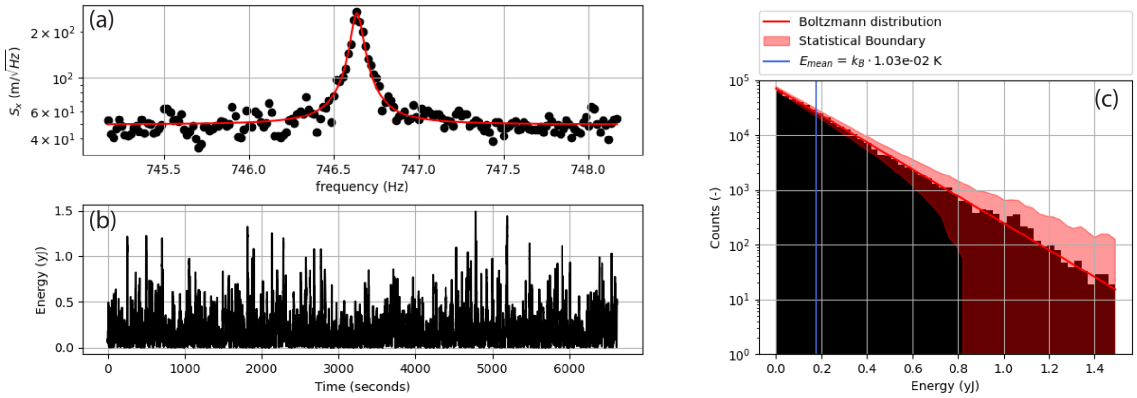

FIG. 2. The cantilever temperature is determined from the readout SQUID signal after post-processing. (a) The resonance frequency of the cantilever is visible as a peak in the amplitude spectral density when the cantilever thermal motion exceeds the (white) detection noise. (b) A digital lock-in amplifier is used at this resonance frequency on the SQUID time signal to obtain the cantilever amplitude as a function of time. (c) After plotting the energy in a histogram, the cantilever temperature is obtained from the mean energy and crosschecked through the slope of the energy distribution. The red shaded area indicates one standard deviation in the number of counts per bin.

cantilever frequency can vary due to local forces, such as Meissner repulsion induced by the superconducting structures of the readout circuit or due to magnetic interactions with surface spins [29, 39]. We measure the effective resonance frequency ω_{eff} by exciting the cantilever magnetically through the calibration coil or mechanically through the piezo and fitting a Lorentzian to the Fourier transform of the SQUID signal (10 minutes of integrated signal is shown in Fig. 2 a).

The (digital) lock-in amplifier is applied to the measured time signal from the readout SQUID at resonance frequency ω_{eff}. We set the lock-in bandwidth to 1 Hz, approximately two times the bandwidth over which the thermal motion of the resonator stands out above the detection noise (see Fig. 2a). The correlation time of the cantilever is $\tau = 2\frac{Q}{\omega_0}$, which determines the timescale at which its energy decays. A value for can be determined by sweeping cantilever excitations around the resonance frequency. Typically we find $\tau \approx 7\,\text{s}$. Hence, two hours of data, as presented in figure 2b, contains about 1028 independent measurements of the cantilever energy, from which we infer the cantilever temperature by taking the mean. To verify the thermal nature of the data, we compare a histogram to the Boltzmann distribution, which scales as: $\sim \exp\left(\frac{E}{k_B T}\right)$ (Fig. 2c). A cutoff is visible (i.e. the number of counts drops abruptly from 25 to zero) at high energy, because the sample rate of the lock-in is much faster than the rate at which the cantilever energy varies, determined by τ.

To crosscheck the temperature, we define an expression for the standard deviation δn of the distribution. Given the number of independent measurements in a bin is equal to t_{bin}/τ, with t_{bin} the bin duration, we expect the relative variation to be:

$$\frac{\delta n}{n_{\text{bin}}} = \frac{1}{\sqrt{t_{\text{bin}}/\tau}}\,, \tag{1}$$

for a bin that contains n_{bin} counts. 95% of the data are expected to fall within an interval of $\pm 2\,\delta n$ around Boltzmann distribution, which is confirmed by our analysis (see Fig. 2c). By fitting the slope of the distribution we extract a cantilever temperature of $10.3(2)\text{mK}$ (where the value between brackets denotes the uncertainty on the last digit).

C. Thermal Motion below 10 mK

The results in this work concern a comparison between two independent datasets of the cantilever temperature. These datasets are used to discuss the factors that cause saturation of the cantilever temperature and factors that cause offsets in the calibration procedure for the cantilever amplitude.

Each dataset consists of a measurement of thermal fluctuations of the cantilever when changing the current through the nuclear demagnetization coil. The field of the nuclear demagnetization coil is first ramped up to 2 T. The energy released during this process is thermalized to the dilution refrigerator through a aluminium heat conductance switch. After the field has reached 2 T and the demagnetization stage has thermalized, the heat conductance switch is flipped to minimize thermal conductivity. Then the field is reduced stepwise, providing cooling power to the silver wire through the demagnetization of the $PrNi_5$. At the lowest magnetic field, the cantilever and detection chip are allowed

to thermalize for at least 12 hours, while the amplitude of the cantilever resonance is being monitored and the MFFT acquires temperature data. When no further decrease in the measured cantilever PSD is observed, we ramp up the current through the nuclear demagnetization in a stepwise fashion, while monitoring the cantilever amplitude. After each step, we wait for the MFFT temperature to reach a stable value after which two hours of data are acquired.

The thermal motion measured in dataset A is plotted as a PSD in figure 3a to be able to observe a decrease in amplitude at lower temperatures. The final temperature is extracted from the corresponding histograms, which can be found in appendix F. During all measurements, the thermal fluctuations of the cantilever can clearly be distinguished from the background detection noise. The measured thermal fluctuations of the cantilever, plotted as a cantilever temperature $T_{\text{cantilever}}$, are plotted against the MFFT temperature T_{MFFT} in figure 3b. Horizontal error bars indicate the standard deviation of the temperature measurements from different spectra throughout this time interval. If the cantilever is in thermal equilibrium, its temperature is expected to fluctuate around an average value $\bar{T}_{\text{avg}}$. The standard deviation of these fluctuations over a time interval t_{meas} is described using $\Delta T = \sqrt{\tau/t_{\text{meas}}}\bar{T}_{\text{avg}}$ around the average temperature.

TABLE I. Parameters of the two different measurement runs. $\mathbf{T_{final}}$ is the lowest temperature measured through the cantilever thermal motion during a run, $\mathbf{T_{MFFT}}$ the lowest temperature measured through the MFFT.

Run	**Frequency** (Hz)	Q (-)	κ (m/V)	$\mathbf{T_{final}}$ (mK)	$\mathbf{T_{MFFT}}$ (mK)
A	746.6	13200 (100)	$9.6(6)\cdot10^{-6}$	6.1(4)	3.4(4)
B	669.7	15400 (400)	$1.9(2)\cdot10^{-5}$	7.7(4)	3.1(2)

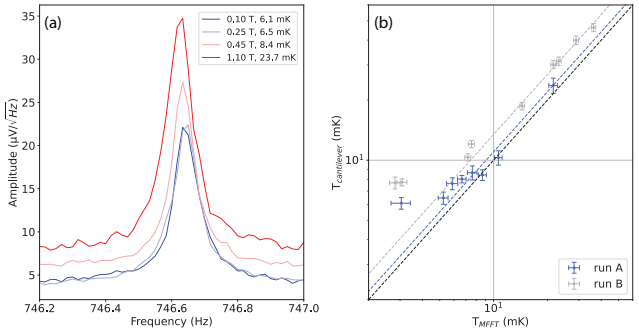

FIG. 3. Temperature determined from the cantilever thermal motion versus bath temperature. (a) shows the thermal motion as observed in the power spectral density during measurement run A at various magnetic fields in the nuclear demagnetization stage. In (b) the cantilever temperature $T_{\text{cantilever}}$ is plotted against the MFFT temperature T_{MFFT} during run A and B. The dashed lines indicate $T_{\text{cantilever}} = cT_{\text{MFFT}}$ corresponding to run A and B. The black dashed line indicates $c = 1$.

Throughout both datasets, we observe that $T_{\text{cantilever}} > T_{\text{MFFT}}$ to within the uncertainty of $T_{\text{cantilever}}$. At the lowest temperatures, $T_{\text{cantilever}}$ is saturated and does not decrease further, at a saturation temperature of $6.1(4)\,\text{mK}$ and $7.7(4)\,\text{mK}$ for run A and B, respectively. Even at the lowest temperatures, the cantilever motion is still following a Boltzmann distribution, hinting at a thermally distributed origin of the saturation.

To quantify the deviation between $T_{\text{cantilever}}$ and T_{MFFT}, we fit $T_{\text{cantilever}} = cT_{\text{MFFT}}$ for the data with $T_{\text{MFFT}} > 8\,\text{mK}$. For the data in run A, the value for $c = 1.08(4)$, close to 1, which is expected when the cantilever and MFFT are well thermalized to each other. However in run B, c is equal to $1.35(4)$. As no changes were made to the silver wire or cantilever between datasets A and B, we suspect the deviation in c is the result of inaccuracies in the displacement calibration of the cantilever. A possible origin is the presence of electrostatic forces driving the cantilever. The calibration only takes into account forces due to generated magnetic fields. However, if there are any residual charges on the cantilever tip, electrostatic forces can act as an additional drive of unknown sign on the cantilever due to parasitic capacitances. Appendix G discusses potential inaccuracies in the displacement calibration in more depth. If the calibration in run B was lower such that $c = 1$, it would result in a saturation temperature around $6\,\text{mK}$, similar to dataset A.

We deem it unlikely that the saturation of the cantilever temperature around $6\,\text{mK}$ is due to external vibrations. Vibrations would result in day-night variations of the cantilever temperature. We do not observe such variations, as is visible in appendix E. We fit the functional $T_{\text{cantilever}} = (T_{\text{MFFT}}^n + T_0^n)^{1/n}$ to the data of run A. The free parameters are the saturation temperature T_0 and coefficient n. The value of n can be used to determine the limiting thermal resistance [40, 41]. This yields $n = 4(2)$ and $T_0 = 6(1)\text{mK}$. This is consistent with a thermal resistance coupled in through the detection chip. A hypothesis is heating due to the thermal dissipation of the DC bias voltage in the SQUID detection circuit.

D. Discussion

Through the use of nuclear demagnetization in combination with a vibration isolation system, we demonstrated passive cooling of a nanomechanical cantilever to temperatures below $10\,\text{mK}$, measuring its equilibrium motion at temperatures down to $6.1(4)\text{mK}$. This result constitutes an important step towards future tests of quantum mechanics. Among these tests are experiments that focus on generation of large non-classical states [42] and experiments that impose bounds on wavefunction collapse models such as CSL [31].

The success of these experiments is dependent on the force noise of the cantilever for which we can make an

estimate using the method of Stowe *et al.* [17]. Our current cantilever has a resonance frequency of approximately $2\pi \cdot 700\,\mathrm{Hz}$, effective mass is $m_{\mathrm{eff}} \approx 1.5\,\mathrm{ng}$ and $Q \approx 14000$. At $6.1\,\mathrm{mK}$ this yields $\sqrt{S_F} \approx 3.9 \times 10^{-19}\,\mathrm{N}/\sqrt{\mathrm{Hz}}$. This is on the same order as the best efforts to optimize force noise in the low-kHz regime [43, 44] and two orders of magnitude higher than the state of the art for clamped mechanical resonators [16, 45].

This figure can be improved by a number of changes to the experiment. The experiments performed by van Heck *et al.*, were carried out with the exact same cantilever, which then had $Q \approx 40000$. It is unclear what caused the deterioration of its Q-factor. A higher Q-factor can be achieved by switching to nanoladder cantilevers [13]. By combining $Q \approx 40000$ with a cantilever temperature of $0.5\,\mathrm{mK}$ we can potentially achieve $6.8 \times 10^{-20}\,\mathrm{N}/\sqrt{\mathrm{Hz}}$.

There are two issues to overcome in order to cool a cantilever down to $0.5\,\mathrm{mK}$. Firstly, one has to remove any mechanisms that currently cause saturation of the cantilever temperature. Potential origins are heating caused by the SQUID detection circuit and free electron spins on the detection chip that are excited by spurious magnetic field fluctuations. Secondly, one can improve the techniques to lower the demagnetization temperature by either increasing the cooling power of the experiment or by reducing the heat input through conduction or mechanical vibrations. This is possible through a second nuclear demagnetization system, utilizing nuclear spins in copper, that is precooled using the existing nuclear demagnetization coil.

Finally, for future experiments, it is important to reduce uncertainty in the calibration procedure. This requires a way to mitigate the effect of parasitic capacitances throughout the magnetic calibration or by reducing any remaining charges on the cantilever, making it less susceptible to the electrostatic driving force.

ACKNOWLEDGMENTS

We would like to thank Maria Luisa Mattana for her valuable feedback on the manuscript.

TO and LvE acknowledge funding from the Netherlands Science Organisation (NWO grant OCENW.GROOT.2019.088) and from two Quantum Delta National Growth Fund grants.

Appendix A: Description of the Experimental Setup

The experimental setup used in this work is described in section A. This section provides more detail on thermal isolation of the mass-spring system and sample holder.

In figure 4 the mass-spring system and the silver wire are shown. To selectively cool the cantilever and the sample chip, the silver wire is routed along a mass-spring system in a manner that does not compromise our mechanical vibration isolation. Specifically, this means that the silver wire is mechanically, but not thermally, connected to every mass of the mass-spring system The silver wire is connected through LEGO® bricks as these have been shown to have a low thermal conductance at milliKelvin temperatures [46].

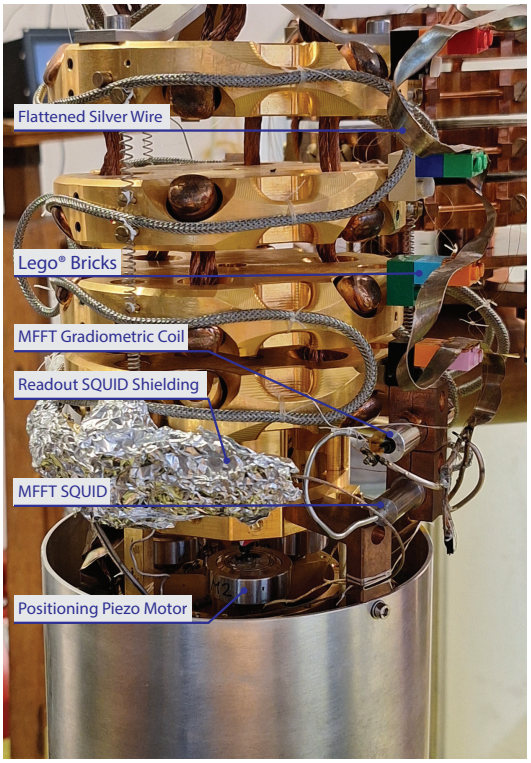

FIG. 4. The experimental setup used during the experiments presented in this work. The MFFT is visible in the lower right part. The lowest part of the setup contains the piezo motors and cantilever. The silver wire can be seen on the right of the image, it is thermally isolated from the mass-spring system by using LEGO® bricks.

Thermal isolation between the detection chip and the sample holder is achieved by placing the detection chip on top of a machined Macor® plate (dimensions $h \times w \times l = 1 \times 20 \times 20$ mm). Macor® has low thermal conductivity at low temperatures (at $< 100\,\mathrm{mK}$) $\kappa \leq 1\,\mu\mathrm{W m^{-1} K^{-1}}$ [47]). The pickup loop chip is glued inside a $500\,\mu\mathrm{m}$ deep indent on the top side of the Macor® plate. The bottom of the Macor® plate contains a $125\,\mu\mathrm{m}$ deep round well to lengthen the thermal path from detection chip to the rest of the sample holder. The secondary side of the transformer chip is

wirebonded to bulk niobium blocks with screw terminals in which the ends of a 35 cm superconducting twisted wire is clamped. The other side of the twisted wire is connected to the detection SQUID that is placed outside the sample holder to prevent the feedback current of the SQUID from affecting the cantilever.

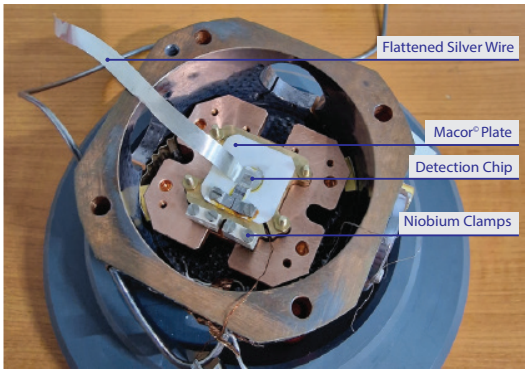

FIG. 5. The sample holder of the instrument. In the center the detection chip can be seen on top of the Macor® plate. The silver wire connected to the nuclear demagnetization stage is also visible.

Appendix B: Calibration of Magnetic Flux Fluctuation Thermometer: Data Analysis

The magnetic flux fluctuation thermometer is used as means to monitor the bath temperature of the cantilever and detection chip. Temperature can be inferred from the MFFT by monitoring the magnetic flux power spectral density (PSD) $S_\Phi(f)$ generated by Johnson-Nyquist noise in the silver wire, which obeys the relation [29]

$$S_\Phi(\omega) = 4k_B T R\sigma\mu_0^2 R^3 G(R/\delta), \tag{B1}$$

with σ the bulk conductivity of the silver wire, μ_0 the magnetic permeativity of vacuum, R the radius of the silver wire and $\delta = \sqrt{\mu_0\sigma\omega}$ the skin depth. The frequency dependence of Σ_Φ enters through $G(R/\delta)$, which is a dimensionless function dependent that strongly depends on the geometry of the MFFT [35]. Unfortunately, van Heck *et al.* [29] demonstrated that our group was unable to find an analytic solution for G. As such, the MFFT requires a calibration to a suitable reference thermometer. We use a calibration that is similar but not the same to the calibration used by van Heck *et al.*.

First the PSD of a measured spectrum is obtained through discrete Fourier transform, using Welch's method. This is done using a Hanning window and 50% overlap between subsequent windows. The resulting spectra are trimmed to only contain frequencies between 50 Hz and 6050 Hz, to reduce the size of the data for processing. This is shown in grey in figure 6a. The spectra contain many peaks, that are the result of interference instead of thermal fluctuations. This interference can be picked up in the wiring before the MFFT SQUID, through crosstalk between the MFFT SQUID and the silver wire or at different places in the MFFT readout chain.

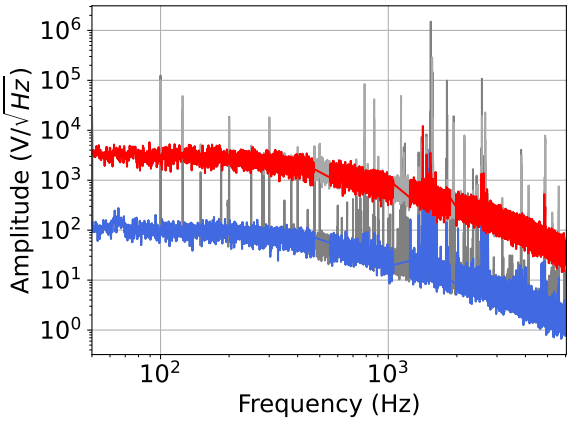

FIG. 6. Data analysis of the magnetic flux fluctuation thermometer (MFFT). The filtered PSD of the MFFT SQUID is plotted between 50 Hz and 6050 Hz, measured at 2.6 mK (blue) and 100 mK (red).

To remove this interference from our temperature measurement mask is made using at spectra that are expected to be low temperature, as interference peaks are often drowned out at higher temperatures. This mask is then applied to all data of a measurement run. This effect is visible in figure 6a. To identify peaks for masking, a spectrum is divided in bins of 500 Hz and a linear fit of the background is made through which the binned frequencies are divided. Then a peakfinder algorithm is applied that filters peaks based on their prominence for at least a 1000 spectra in a run. If a frequency is marked as a peak in at least 1.5% of these spectra, it is discarded. The con of this method is that interference with a width comparable to the bin width, are not picked up. Therefore, any broad peaks are masked by hand and discarded.

The actual calibration is done using the spectral noise power

$$P = \int_{\omega_1}^{\omega_2} S_\Phi(\omega)\, d\omega, \tag{B2}$$

when integrating along a frequency band between ω_0 and ω_1. This is a quantity that varies linearly with temperature, which is essential for a primary thermometer. Spectral noise power is calculated from the spectra by doing a numeric intergration between $\omega_1 = 50$ Hz and $\omega_2 = 6050$ Hz. A linear fit of P is made with respect to the reference thermometer when the reference thermometer gradually increased or decreased over at least a day to ensure that the silver wire has a constant temperature and that the

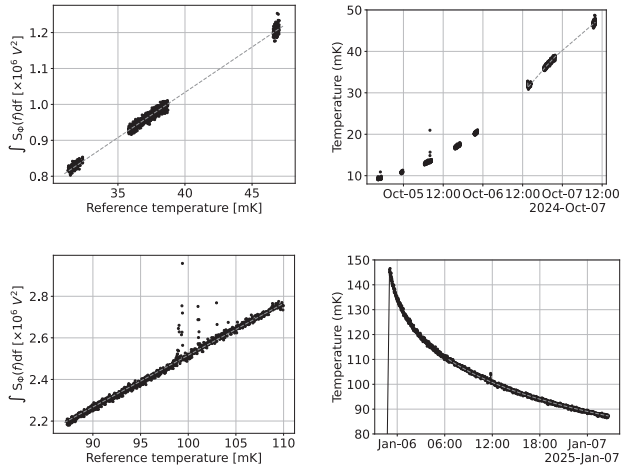

FIG. 7. In the left column, the conversion between spectral noise power P in this band and the resistive reference thermometer is plotted for run A (a) and B (c). A linear dependence between P and the reference temperature can be observed. In the right column, the temperature data that is used to calibrate the MFFT is plotted for run A (b) and B (d). The MFFT temperature (black dots) follows the temperature from resistive reference thermometer (grey dashes) during this period.

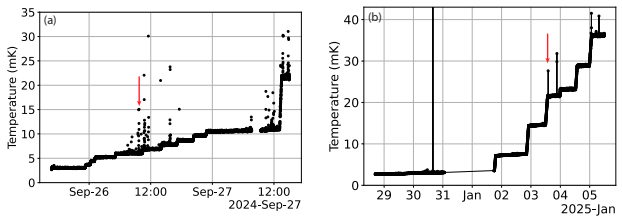

FIG. 8. Temperature measured through the MFFT during run A (a) and B (b). Red arrows indicate spikes in temperature of the SQUID. It is unclear what the origin of these spikes is.

reference thermometer is well thermalized. The resulting calibration is shown in figure 7a 7c . We use data between 15 mK and 1 K as the reference thermometer is calibrated in this range. The exact temperatures per measurement run are indicated in table II. Variations in the slope is the result of different tuning of the MFFT SQUID. The MFFT SQUID is operated at a constant flux bias, which is kept constant using a feedback loop. This feedback loop is tuned at the beginning of a measurement run, during which slight variations in the magnetic background can result in a different sensitivity to magnetic flux. The calibration is subsequently applied to all data of a measurement run.

Subsequently, the obtained calibration of the MFFT is applied to all measured MFFT spectra. The result is plotted for both datasets in figure 8. The steps in current are correlated with increments of the current through the nuclear demagnetization coil. In 8 we can observe peaks at several moments. We attribute these to mechanical excitations of the setup. These vibrations can be transmitted to the silver wire and cause the MFFT to temporarily show a strong increase in temperature. We observe that these peaks only occur during daytime, which is also seen by van Heck *et al.* [29]. Beside occasional excitations, there is no day-night variation visible in the measured temperatures.

The uncertainty on the obtained temperature T_{MFFT} is calculated for the 2-hour intervals on which we determined the cantilever temperature in figure 3 of the main text. This was done by taking the spectra measured during each interval and calculating the temperature T_{MFFT} from each individual spectrum. This results in at least $N = 119$ spectra for each time interval. These temperature measurements can be binned to obtain a histogram. We then fitted a Gaussian distribution $f(x) = \frac{1}{\sqrt{2\pi}\sigma} e^{-\frac{1}{2}\left(\frac{x-\mu}{\sigma}\right)^2}$, with μ and σ respectively the center and the width of the distribution. The uncertainty on the temperature measurement was then taken to be equal to two times the width σ.

Appendix C: Cantilever Thermal Motion: Displacement Calibration

Our detection method is based on detecting a change of flux inside a pickup loop. Due to this change in flux, a current will flow through a two-stage detection circuit which also includes a measurement SQUID, shown in figure 9. At the output of the detection circuit, a voltage is measured. In order to convert this measured voltage to motion of the resonator, we need to obtain a coupling factor that relates both quantities. This procedure allows to calibrate the amplitude of cantilever oscillations independently of a measured bath temperature.

This displacement calibration is similar to the one applied in [9, 29]. The cantilever is driven through insertion of an oscillating test flux $\Phi_{\mathrm{crosstalk}}$ in a calibration coil between the pickup loop and the detection SQUID. This flux can be measured directly from the detection SQUID, but also excites the cantilever motion, which results in an oscillating flux Φ_{motion}. For a small test flux $\Phi_{\mathrm{crosstalk}}$, the flux change Φ_{motion} is approximately linear to the cantilever displacement. As such, a transfer function between cantilever displacement x and flux Φ_{motion} can be derived. Taking into account the SQUID detection circuit, we can obtain the conversion parameter κ, which describes the voltage generated by the detection circuit per flux quantum induced in the pickup loop.

The first part of this appendix introduces a model for the different inductances in our detection circuit. Then we derive a relation between the motion of the cantilever and the induced voltage in the SQUID and present the practical implementation and limitations of this displacement calibration method. Lastly, we discuss the introduction of potential

TABLE II. The parameters that were used to calibrate the MFFT during different measurements

Run	Start Date	Finish Date	Sampling Rate (Sa/s)	File length (s)	Total files	slope m ($\mu\Phi_0/mK$)
A	23/9/2024	7/10/2024	2000000	16	13664	$2.5e4$
B	29/12/2024	7/1/2025	500000	61	11489	$2.3e4$

sources of uncertainty during this calibration.

1. Inductance of a Two-stage Detection Circuit

For the calibration flux is injected in this circuit using the calibration coil, in the right half of the circuit in figure 9. We can start the analysis by considering a voltage over the right part of the circuit (the part directly connected to the SQUID). From figure 9 we see

$$U_{\text{in}} = i\omega L_{\text{t2}} I_{\text{in}} - i\omega M_{12} I_{\text{out}} \tag{C1}$$

for the 'primary circuit' and for the 'secondary circuit'

$$i\omega M_{12} I_{\text{in}} = I_{\text{out}}(i\omega L_{\text{t1}} + Z_{\text{pl,par}}), \tag{C2}$$

with $Z_{\text{pl,par}} = i\omega L_{\text{pl}} + i\omega L_{\text{par,1}}$. Combining these equations yields

$$Z_{\text{sec}} = \frac{U_{\text{in}}}{I_{\text{in}}} = i\omega\left(L_{\text{t2}} - \frac{M_{12}^2}{L_{\text{t1}} + L_{\text{pl}} + L_{\text{par,1}}}\right). \tag{C3}$$

Since $Z_{\text{sec}} = i\omega L_{\text{sec}}$, we obtain for the whole circuit

$$\begin{aligned} L_{\text{tot}} &= L_{\text{fi}} + L_{\text{inp}} + L_{\text{par,2}} + L_{\text{sec}} \\ &= L_{\text{fi}} + L_{\text{inp}} + L_{\text{par,2}} + L_{\text{t2}} - \frac{M_{12}^2}{L_{\text{t1}} + L_{\text{pl}} + L_{\text{par,1}}}. \end{aligned} \tag{C4}$$

So for a two-stage detection circuit we should use equation C4 for the total inductance.

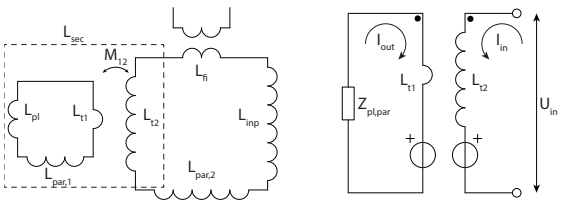

FIG. 9. *Left* shows the two-stage detection circuit we use, the pickup loop (L_{pl}) is connected to a transformer (L_{t1} and L_{t2}) which is connected to the circuit that also includes the input coil (L_{inp}) of the SQUID and the flux injection coil (L_{fi}). On the *right* a simplified version of this diagram is shown which focuses only on the part inside the dotted rectangle on the left figure.

2. Energy Coupling Between SQUID and Resonator

As a next step, we derive the coupling between the cantilever displacement and the voltage measured at the output of the two-stage detection circuit. First we require the coupling from measured voltage to flux in SQUID loop, which we obtain from the manufacturer. Secondly, we derive the coupling between the motion of the cantilever and the amount of flux in SQUID loop. The following derivation is based on the analysis described by Fuchs *et al.* [9]. We define the coupling strength β as the square root of the ratio of the energy in the circuit and the energy in the cantilever mode, equivalently

$$\beta^2 = \frac{L_{\text{tot}} I^2}{kx^2}. \tag{C5}$$

With L_{tot} the total inductance of the detection circuit, I the current through that circuit, k the spring constant of the cantilever and x the position of the cantilever with respect to its equilibrium position. By substituting $k = m\omega^2$ and $I = \frac{\Phi}{L_{\text{tot}}}$ we obtain

$$\beta^2 = \frac{(\frac{d\Phi}{dx})^2}{L_{\text{tot}} m\omega^2}. \tag{C6}$$

By sending an oscillating signal through the calibration coil, part of the current $I_{\text{crosstalk}}$ will go to the pickup loop and exert a driving force on the cantilever that can be written as

$$F_{\text{drive}} = \alpha I_{\text{crosstalk}}. \tag{C7}$$

Here we introduced a factor α with units $\frac{\text{N}}{\text{A}}$ that depends on the geometry of the pickup loop and the position of the cantilever with respect to the pickup loop. As the cantilever gets driven by this force, it will eventually reach equilibrium as the driving force becomes equal to the damping force which is given by

$$F_{\text{damping}} = \gamma \frac{dx}{dt} = \gamma\omega x, \tag{C8}$$

with $\gamma = \frac{m\omega}{Q}$ the damping factor. The driven cantilever now also generates a changing flux in the pickup loop causing a current I_{drive} to flow through the detection circuit given by

$$I_{\text{drive}} = \delta \cdot x. \tag{C9}$$

The introduced coupling factor δ with units [A/m] depends on the geometry of the system in the same way as α. For small amplitude of the cantilever motion, we can linearize the flux change through the pickup loop as function of cantilever position x, such that

$$I_{\text{drive}} = \frac{d\Phi}{dx}\frac{1}{L_{\text{tot}}} x. \tag{C10}$$

As the currents $I_{\text{crosstalk}}$ and I_{drive} occupy the same part of the circuit, they should depend on the circuit geometry in the same way. Therefore, α should have the same geometry factor as δ and we obtain

$$\alpha = \frac{d\Phi}{dx}. \tag{C11}$$

We notice that the unit of α are $[\text{Wb/m}] = [\text{N/A}]$, consistent with equation C7. Dividing the drive current by the crosstalk current, yields

$$\frac{I_{\text{drive}}}{I_{\text{crosstalk}}} = \frac{\alpha\delta x}{F_{\text{drive}}} = \frac{(\frac{d\Phi}{dx})^2 x}{L_{\text{tot}} F_{\text{drive}}}. \tag{C12}$$

At equilibrium ($F_{\text{drive}} = F_{\text{damping}}$) this can be rewritten as

$$\frac{I_{\text{drive}}}{I_{\text{crosstalk}}} = Q\frac{(\frac{d\Phi}{dx})^2}{L_{\text{tot}} m\omega^2} = Q\beta^2. \tag{C13}$$

The second equality shows that this fraction is equal to the coupling strength multiplied by the Q-factor. In order to obtain a measure for the coupling between the cantilever motion and flux in the detection circuit, we can write

$$\frac{d\Phi}{dx} = \sqrt{\frac{1}{Q} L_{\text{tot}} m\omega^2 \frac{I_{\text{drive}}}{I_{\text{crosstalk}}}}. \tag{C14}$$

From equation C14 we can observe that a measuremnent of the displacement sensitivity requires measuring the fraction $\frac{I_{\text{drive}}}{I_{\text{crosstalk}}}$. As both currents pass through the same part of the detection circuit, it is equal ot the ratio of the measured voltages V_{drive} and $V_{\text{crosstalk}}$, by an equal coupling factor. This allows to rewrite equation C14 as

$$\frac{d\Phi}{dx} = \sqrt{\frac{1}{Q} L_{\text{tot}} m\omega^2 \frac{V_{\text{drive}}}{V_{\text{crosstalk}}}}. \tag{C15}$$

In this equation, the quantity to be measured is $\frac{V_{\text{drive}}}{V_{\text{crosstalk}}}$. The next section details the measuring procedure.

3. Implementation of Displacement Calibration

The fraction $\frac{V_{\text{drive}}}{V_{\text{crosstalk}}}$ is measured by doing a frequency sweep through the calibration loop around the resonator resonance frequency. Figure 10 (a) shows the result of such a sweep in the complex plane. A circle arises due to excitation of the cantilever around its resonance. This circle diameter is equal to V_{drive}. The corresponding PSD is expected to have a Lorentzian lineshape

$$S(\omega) = \frac{A}{(\omega - \omega_0)^2 + (\gamma/2)^2}, \tag{C16}$$

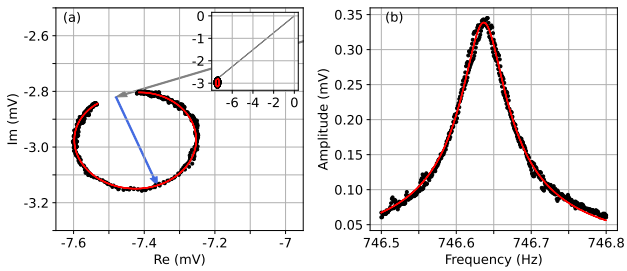

FIG. 10. A frequency sweep for which the cantilever is driven magnetically through the calibration coil. (a) shows the measured cantilever resonance in the complex plane. At each frequency a complex voltage (blue) is measured, which contains amplitude and phase information. Two vectors illustrate the amplitude of the resonance (red) and crosstalk (green). The resonance is fitted to a Lorentzian (orange). The inset shows the resonance with respect to the origin. In (b) the power spectral density (blue) and corresponding Lorentzian fit (orange) are plotted.

with A the amplitude and γ the with of the peak. The circle diameter equals V_{drive} and is fitted with equation C16 plus a constant offset. Due to the direct crosstalk between the calibration coil and the SQUID, the circle is not located at origin. The resulting offset is plotted as a vector in figure 10, with an amplitude that is equal to $V_{\text{crosstalk}}$. Thus, the coupling strength β can be inferred from the length ratio of both vectors.

To relate β and α to the measured voltage, we introduce a parameter $\kappa = \frac{\text{dV}}{\text{dx}}$. We observe that $\alpha = \frac{d\Phi}{dx}$ determines the flux change in the pickup loop due to the sweeping current $I_{\text{crosstalk}}$. It can be related to the flux change in the pickup loop through

$$\kappa = \frac{dV}{dx} = \frac{dV}{d\Phi_{\text{SQ}}} \cdot \frac{d\Phi_{\text{SQ}}}{dI} \cdot \frac{dI}{d\Phi} \cdot \frac{d\Phi}{dx} \tag{C17}$$

The current change in the detection circuit $\frac{dI}{d\Phi}$ equals the reciprocal of the total inductance $\frac{1}{L_{\text{tot}}}$. The SQUID is calibrated to have a mutual inductance $\frac{d\Phi_{\text{SQ}}}{dI} = 5 \cdot 10^{-7}\text{A}/\Phi_0$ and voltage gain $\frac{dV}{d\Phi_{\text{SQ}}} = 0.43\text{V}/\Phi_0$. The coupling strength β and conversion parameter κ are given in table I of the main text for the measurement runs presented in this work. The uncertainty in the κ varies between 6% for run A and 11% for run B. Take note that this entails the uncertainty due to the fitting parameters f_0, γ and A. It does not account for systematic errors as discussed in the results of this work, such as any additional electrostatic driving or voltage noise .

The measured conversion parameters κ and $Q\beta^2$ is given in section C 4. The sweeps that are used to obtain the respective values are plotted in figure 11.

4. Measurements of Energy Coupling

In table III of appendix E the parameters relevant to the measured coupling during run A and B are shown. The sweep that was used during the displacement calibration in these runs are shown in figure 11.

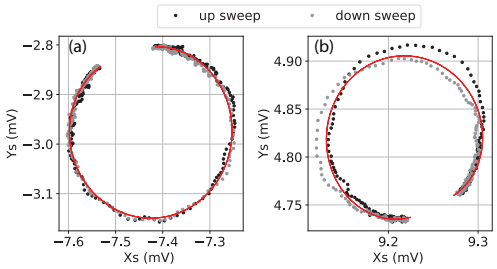

FIG. 11. Sweeps of a magnetic flux through the calibration coil to obtain the coupling. Black and grey dots distinguish between measurements when the frequency is respectively swept up or down. Red is obtained from a Lorentzian fit of the voltage amplitude of the data as a function of frequency. From (a) the coupling was measured to be $\kappa = 9.6(6) \cdot 10^{-6}$ V/m during run A. From (b) the coupling in run B was measured to be $\kappa = 1.9(2) \cdot 10^{-5}$ V/m.

Appendix D: Digital Lock-in Amplifier Procedure

This appendix sets apart the procedure that was used to apply a digital lock-in amplifier to the measured cantilever signal at a frequency ω_0. This enables us to extract the cantilever amplitude and energy as a function of time.

As a starting point, we take the measured voltage signal from the detection SQUID as a function of time. To obtain the in-phase (out-of-phase) quadrature of this signal, we multiply by $\cos(\omega_0 t)$ ($\sin(\omega_0 t)$). To both quadrature signals a low-pass filter is applied, which has a cutoff frequency that is set by the ratio of the lock-in bandwidth over the measurement frequency of the original signal. Finally, the filtered quadrature signals are recombined to obtain a complex voltage signal. This signal is then averaged over a period that is determined by the lock-in sample rate. This period is the inverse of this sample rate.

To account for the background that is present in the original signal, the same procedure is then repeated with a lock-in at both $\pm 5\,\mathrm{Hertz}$ from ω_0.

Appendix E: Combined MFFT and Cantilever Temperature Data

The combined temperature measurement through the MFFT and the temperature measured from the cantilever motion are displayed in figure 12. In table III contains the parameters resulting from the displacement calibration (details outlined in the supplementary material [36]).

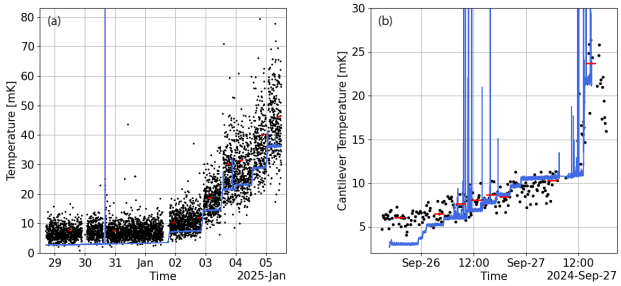

FIG. 12. Temperature steps measured during run A (a) and B (b). The temperature of the MFFT is plotted in blue and the cantilever temperature in black. Red bars indicate the time segments used to calculate the datapoints in figure 3 (b) of the main text.

Appendix F: Thermal Distributions of Cantilever Motion

In figure 13 the histograms of the cantilever energy corresponding to the curves in figure 3a are plotted. As indicated in the results section, variations in the cantilever energy occur over an interval determined by the inverse cantilever time constant$1/\tau$. This is much slower than the sample rate of the digital lock-in amplifier, which is 100 Sa/s. As a result, bins with less than $\tau/10 * 100\,\mathrm{Sa/s} \approx 70$ counts have little statistical significance.

Appendix G: Offset in the Cantilever Temperature Conversion

To obtain a quantified measurement of the cantilever temperature, several data processing steps are relevant. Here we discuss several issues that we identified in this procedure. Any inaccuracy can result in both a too low or too high figure for the cantilever temperature. We first present a potential systematic error due to deviations in the mass of the cantilever tip. Then we discuss the effect of electrostatic driving of the cantilever during the displacement calibration.

From the measured amplitude of the cantilever oscillations, the cantilever energy is calculated using a proportionality constant $E \propto m_{\mathrm{eff}}\omega^2$. The energy thus scales linearly with the effective cantilever mass, which is dominated by the mass of the spherical magnetic tip. We now discuss the uncertainty in the mass of this magnetic tip. The tip diameter was observed to be $7.3\,\mu\mathrm{m}$, using a scanning electron microscope. We assume that this value is precise to about 8%. Using the density of $Nd_2Fe_{14}B$ ($\rho = 7450\,\mathrm{kg/m^3}$) we find that this translates to a mass of the tip of $1.51(35)\,\mathrm{ng}$. The cantilever mass is around $0.12\,\mathrm{ng}$. Taking into account the uncertainty in the mass of

TABLE III. Parameters for the cantilever displacement calibration as measured for the different runs in this work. Sample rate refers to the sample rate of the detection SQUID, The paramaters β and κ are respectively the energy coupling and conversion parameter from the displacement calibration. The temperatures $\mathbf{T_{final}}$ and $\mathbf{T_{MFFT}}$ are the lowest temperatures measured on from the cantilever motion and through the MFFT respectively.

Run	**Sample Rate** (Sa/s)	**Frequency** (Hz)	Q (-)	β (-)	$Q\beta^2$ (-)	κ (m/V)	$\mathbf{T_{final}}$ (mK)	$\mathbf{T_{MFFT}}$ (mK)
A	50000	746.6	13200 (120)	$1.8(6) \cdot 10^{-3}$	$4.4(6) \cdot 10^{-2}$	$9.6(6) \cdot 10^{-6}$	6.1(4)	3.4(4)
B	6/21/2584	669.7	15400 (400)	$1.0(5) \cdot 10^{-3}$	$1.6(4) \cdot 10^{-2}$	$1.9(2) \cdot 10^{-5}$	7.7(4)	3.1(2)

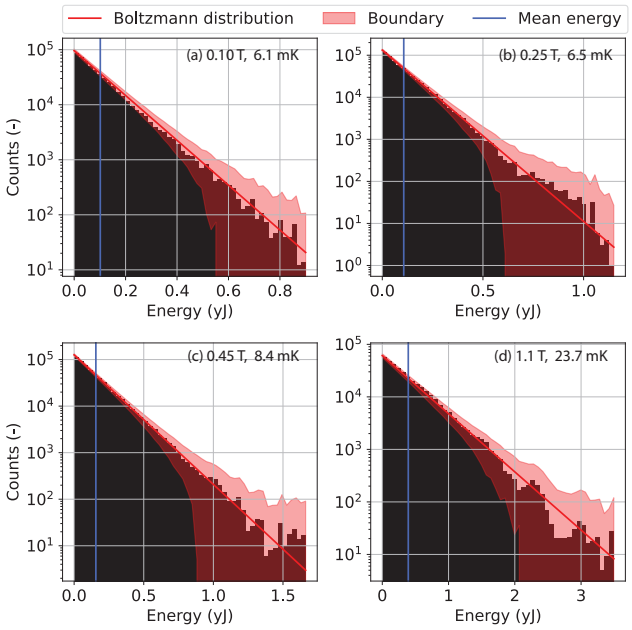

FIG. 13. The histograms of the cantilever motion after applying a digital lock-in amplifier of the curves in figure 3 (a) in the main text. The red line marks the expected number of counts in each bin if they are drawn from a Boltzmann distribution with a width determined by the temperature as calculated from the mean energy. The red shaded area marks one standard deviation around this distribution.

the tip, the uncertainty in the effective mass is found to be on the order of 23%. This directly translates to a systematic uncertainty in the cantilever temperature, as $T_{\text{cantilever}} \propto m$.

We observed that it was possible to electrostatically drive the cantilever through the calibration coil. Figure 14 shows a sweep through the calibration coil, during which the output of the lockin amplifier was grounded on two sides. This means that no current can run through the calibration coil and any effect is due to voltage changes. However, the cantilever is still resonantly driven during this sweep. This indicates that the cantilever tip contains a non-zero electric charge, which is possibly acquired due to a touch of the detection chip while positioning. If electrostatic driving happens in parallel to inductive driving, the measured energy coupling β^2 can deviate from purely inductive driving. If the resulting conversion parameter α is too high or too low, depends on the phase difference with which both driving mechanisms act on the cantilever. It was not possible to calculate the coupling off this effect using the procedure outlined in the supplementary material [36], as no offset flux is present during the SQUID measurement. This suggests there the SQUID signal is not affected through inductive driving during this measurement.

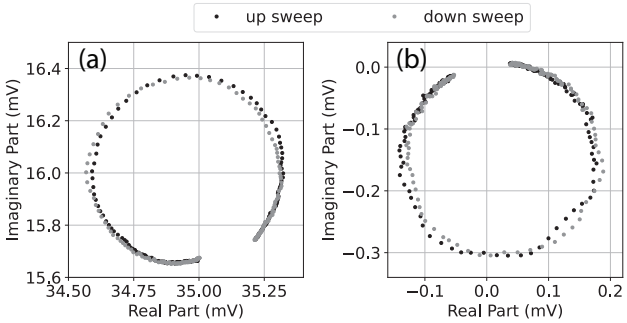

FIG. 14. Two frequency sweeps through the calibration coil. In figure (a) the sweep is conducted in the normal, with the input of the calibration coil connected to the output of the current source. In (b) is conducted to only allow for electrostatic driving of the cantilever. In both figures a circle is visible that the cantilever is excited resonantly. However, in (b) there is no net offset of the circle from the origin, as there is no magnetic flux going through the calibration coil. Additionally, the circle is rotated with respect to the sweep conducted in (a).

[1] A. Vinante, A. Pontin, M. Rashid, M. Toroš, P. Barker, and H. Ulbricht, Testing collapse models with levitated nanoparticles: Detection challenge, Physical Review A **100**, 012119 (2019).
[2] S. Nimmrichter and K. Hornberger, Macroscopicity of mechanical quantum superposition states, Physical review letters **110**, 160403 (2013).
[3] J. Oppenheim, C. Sparaciari, B. Šoda, and Z. Weller-Davies, Gravitationally induced decoherence vs space-time diffusion:

testing the quantum nature of gravity, Nature Communications **14**, 7910 (2023).
[4] S. Bose, I. Fuentes, A. A. Geraci, S. M. Khan, S. Qvarfort, M. Rademacher, M. Rashid, M. Toroš, H. Ulbricht, and C. C. Wanjura, Massive quantum systems as interfaces of quantum mechanics and gravity, Reviews of Modern Physics **97**, 015003 (2025).
[5] B. Schrinski, Y. Yang, U. Von Lüpke, M. Bild, Y. Chu, K. Hornberger, S. Nimmrichter, and M. Fadel, Macroscopic quantum test with bulk acoustic wave resonators, Physical review letters **130**, 133604 (2023).
[6] Y. Y. Fein, P. Geyer, P. Zwick, F. Kiałka, S. Pedalino, M. Mayor, S. Gerlich, and M. Arndt, Quantum superposition of molecules beyond 25 kda, Nature Physics **15**, 1242 (2019).
[7] M. Bild, M. Fadel, Y. Yang, U. Von Lüpke, P. Martin, A. Bruno, and Y. Chu, Schrödinger cat states of a 16-microgram mechanical oscillator, Science **380**, 274 (2023).
[8] T. Westphal, H. Hepach, J. Pfaff, and M. Aspelmeyer, Measurement of gravitational coupling between millimetre-sized masses, Nature **591**, 225 (2021).
[9] T. M. Fuchs, D. G. Uitenbroek, J. Plugge, N. van Halteren, J.-P. van Soest, A. Vinante, H. Ulbricht, and T. H. Oosterkamp, Measuring gravity with milligram levitated masses, Science Advances **10**, eadk2949 (2024).
[10] A. Eichler, Ultra-high-q nanomechanical resonators for force sensing, Materials for Quantum Technology **2**, 043001 (2022).
[11] Y. Seis, T. Capelle, E. Langman, S. Saarinen, E. Planz, and A. Schliesser, Ground state cooling of an ultracoherent electromechanical system, Nature communications **13**, 1507 (2022).
[12] M. Janse, D. G. Uitenbroek, L. van Everdingen, J. Plugge, B. Hensen, and T. H. Oosterkamp, Current experimental upper bounds on spacetime diffusion, Phys. Rev. Res. **6**, 033076 (2024).
[13] M. Héritier, A. Eichler, Y. Pan, U. Grob, I. Shorubalko, M. D. Krass, Y. Tao, and C. L. Degen, Nanoladder cantilevers made from diamond and silicon, Nano letters **18**, 1814 (2018).
[14] T. Gisler, M. Helal, D. Sabonis, U. Grob, M. Héritier, C. L. Degen, A. H. Ghadimi, and A. Eichler, Soft-clamped silicon nitride string resonators at millikelvin temperatures, Physical Review Letters **129**, 104301 (2022).
[15] D. Lee, S. Jahanbani, J. Kramer, R. Lu, and K. Lai, Nanoscale imaging of super-high-frequency microelectromechanical resonators with femtometer sensitivity, Nature Communications **14**, 1188 (2023).
[16] S. De Bonis, C. Urgell, W. Yang, C. Samanta, A. Noury, J. Vergara-Cruz, Q. Dong, Y. Jin, and A. Bachtold, Ultrasensitive displacement noise measurement of carbon nanotube mechanical resonators, Nano letters **18**, 5324 (2018).
[17] T. D. Stowe, K. Yasumura, T. W. Kenny, D. Botkin, K. Wago, and D. Rugar, Attonewton force detection using ultrathin silicon cantilevers, Applied Physics Letters **71**, 288 (1997), https://pubs.aip.org/aip/apl/article-pdf/71/2/288/18527777/288_1_online.pdf.
[18] D. Zoepfl, M. Juan, N. Diaz-Naufal, C. Schneider, L. Deeg, A. Sharafiev, A. Metelmann, and G. Kirchmair, Kerr enhanced backaction cooling in magnetomechanics, Physical Review Letters **130**, 033601 (2023).
[19] A. Youssefi, S. Kono, M. Chegnizadeh, and T. J. Kippenberg, A squeezed mechanical oscillator with millisecond quantum decoherence, Nature Physics **19**, 1697 (2023).
[20] J. D. Teufel, T. Donner, D. Li, J. W. Harlow, M. Allman, K. Cicak, A. J. Sirois, J. D. Whittaker, K. W. Lehnert, and R. W. Simmonds, Sideband cooling of micromechanical motion to the quantum ground state, Nature **475**, 359 (2011).
[21] U. Delić, M. Reisenbauer, K. Dare, D. Grass, V. Vuletić, N. Kiesel, and M. Aspelmeyer, Cooling of a levitated nanoparticle to the motional quantum ground state, Science **367**, 892 (2020).
[22] J. Guo, R. Norte, and S. Gröblacher, Feedback cooling of a room temperature mechanical oscillator close to its motional ground state, Physical review letters **123**, 223602 (2019).
[23] A. D. O'Connell, M. Hofheinz, M. Ansmann, R. C. Bialczak, M. Lenander, E. Lucero, M. Neeley, D. Sank, H. Wang, M. Weides, *et al.*, Quantum ground state and single-phonon control of a mechanical resonator, Nature **464**, 697 (2010).
[24] M. Sarsby, N. Yurttagül, and A. Geresdi, 500 microkelvin nanoelectronics, Nature communications **11**, 1492 (2020).
[25] G. Batey, A. Casey, M. Cuthbert, A. Matthews, J. Saunders, and A. Shibahara, A microkelvin cryogen-free experimental platform with integrated noise thermometry, New Journal of Physics **15**, 113034 (2013).
[26] D. Cattiaux, I. Golokolenov, S. Kumar, M. Sillanpää, L. Mercier de Lépinay, R. Gazizulin, X. Zhou, A. Armour, O. Bourgeois, A. Fefferman, *et al.*, A macroscopic object passively cooled into its quantum ground state of motion beyond single-mode cooling, Nature communications **12**, 6182 (2021).
[27] G. Pickett and C. Enss, The european microkelvin platform, Nature Reviews Materials **3**, 1 (2018).
[28] O. Maillet, D. Cattiaux, X. Zhou, R. R. Gazizulin, O. Bourgeois, A. D. Fefferman, and E. Collin, Nanomechanical damping via electron-assisted relaxation of two-level systems, Physical Review B **107**, 064104 (2023).
[29] B. van Heck, T. M. Fuchs, J. Plugge, W. A. Bosch, and T. H. Oosterkamp, Magnetic Cooling and Vibration Isolation of a Sub-kHz Mechanical Resonator, J Low Temp Phys **210**, 588 (2023).
[30] F. Monteiro, W. Li, G. Afek, C.-l. Li, M. Mossman, and D. C. Moore, Force and acceleration sensing with optically levitated nanogram masses at microkelvin temperatures, Physical Review A **101**, 053835 (2020).
[31] M. Carlesso, S. Donadi, L. Ferialdi, M. Paternostro, H. Ulbricht, and A. Bassi, Present status and future challenges of non-interferometric tests of collapse models, Nature Physics **18**, 243 (2022).
[32] A. Bassi, K. Lochan, S. Satin, T. P. Singh, and H. Ulbricht, Models of wave-function collapse, underlying theories, and experimental tests, Rev. Mod. Phys. **85**, 471 (2013).
[33] A. Vinante, M. Bahrami, A. Bassi, O. Usenko, G. Wijts, and T. Oosterkamp, Upper Bounds on Spontaneous Wave-Function Collapse Models Using Millikelvin-Cooled Nanocantilevers, Physical Review Letters **116**, 090402 (2016).
[34] B. W. Chui, Y. Hishinuma, R. Budakian, H. J. Mamin, T. W. Kenny, and D. Rugar, Mass-loaded cantilevers with suppressed higher-order modes for magnetic resonance force microscopy, Review of Modern Physics **67**, 249 (1995).
[35] A. Fleischmann, A. Reiser, and C. Enss, Noise thermometry for ultralow temperatures, Journal of Low Temperature Physics **201**, 803 (2020).
[36] See Supplemental Material at [URL-will-be-inserted-by-publisher] for details on experimental setup, the displacement calibration and MFFT thermometry.
[37] O. Usenko, A. Vinante, G. Wijts, and T. Oosterkamp, A superconducting quantum interference device based read-out of a subattonewton force sensor operating at millikelvin temperatures, Applied Physics Letters **98** (2011).
[38] J. Wagenaar, *Magnetic Resonance Force Microscopy for Condensed Matter*, Ph.D. thesis, Leiden University (2017), open access at https://hdl.handle.net/1887/50492.
[39] A. M. J. den Haan, J. J. T. Wagenaar, J. M. de Voogd, G. Kon-

ing, and T. H. Oosterkamp, Spin-mediated dissipation and frequency shifts of a cantilever at millikelvin temperatures, Phys. Rev. B **92**, 235441 (2015).

[40] O. Usenko, A. Vinante, G. Wijts, and T. Oosterkamp, A squid based read-out of sub-attonewton force sensor operating at millikelvin temperatures, arXiv preprint arXiv:1007.1572 (2010).

[41] F. Pobell, *Matter and methods at low temperatures*, Vol. 2 (Springer, 2007).

[42] M. F. Gely and G. A. Steele, Superconducting electromechanics to test diósi–penrose effects of general relativity in massive superpositions, AVS Quantum Science **3**, 035601 (2021), https://pubs.aip.org/avs/aqs/article-pdf/doi/10.1116/5.0050988/19738649/035601_1_online.pdf.

[43] G. Ranjit, M. Cunningham, K. Casey, and A. A. Geraci, Zeptonewton force sensing with nanospheres in an optical lattice, Physical Review A **93**, 053801 (2016).

[44] H. Mamin and D. Rugar, Sub-attonewton force detection at millikelvin temperatures, Applied Physics Letters **79**, 3358 (2001).

[45] F. Fogliano, B. Besga, A. Reigue, L. Mercier de Lépinay, P. Heringlake, C. Gouriou, E. Eyraud, W. Wernsdorfer, B. Pigeau, and O. Arcizet, Ultrasensitive nano-optomechanical force sensor operated at dilution temperatures, Nature Communications **12**, 4124 (2021).

[46] J. Chawner, A. Jones, M. Noble, G. Pickett, V. Tsepelin, and D. Zmeev, LEGO® block structures as a sub-kelvin thermal insulator, Scientific Reports **9**, 1 (2019).

[47] A. L. Woodcraft and A. Gray, A low temperature thermal conductivity database, AIP Conference Proceedings **1185**, 681 (2009).